

Supporting Information

Surface oxygenation induced strong interaction between Pd catalyst and functional support for zinc-air batteries

Wei Zhang^{1,2}, Jinfa Chang¹, Guanzhi Wang^{1,2}, Zhao Li^{1,2}, Maoyu Wang³, Yuanmin Zhu^{4,5}, Boyang Li⁶, Hua Zhou⁷, Guofeng Wang⁶, Meng Gu⁵, Zhenxing Feng^{3}, and Yang Yang^{1,2,8,9*}*

1. NanoScience Technology Center, University of Central Florida, Orlando, FL 32826, USA.
Email: Yang.Yang@ucf.edu
2. Department of Materials Science and Engineering, University of Central Florida, Orlando, FL 32826, USA.
3. School of Chemical, Biological, and Environmental Engineering, Oregon State University, Corvallis, OR 97331, USA. E-mail: zhenxing.feng@oregonstate.edu
4. Department of Materials Science and Engineering, Dongguan University of Technology, Dongguan 523808, China
5. Department of Materials Science and Engineering, Southern University of Science and Technology, Shenzhen 518055, China.
6. Department of Mechanical Engineering and Materials Science, University of Pittsburgh, Pittsburgh, PA 15261, USA.
7. X-ray Science Division, Argonne National Laboratory, Lemont, IL 60439, USA
8. Renewable Energy and Chemical Transformation Cluster, University of Central Florida, Orlando, FL 32826, USA.
9. Department of Chemistry, University of Central Florida, Orlando, FL 32826, USA.

Experimental Section

Chemicals

Palladium chloride (PdCl_2 , 98%, TCI America), hydrochloric acid (HCl, AR, Fisher Scientific), nickel sulfate hexahydrate ($\text{NiSO}_4 \cdot 6\text{H}_2\text{O}$, 98%, Alfa Aesar), nickel (II) chloride hexahydrate ($\text{NiCl}_2 \cdot 6\text{H}_2\text{O}$, 97%, Acros Organics), manganese (II) sulfate monohydrate ($\text{MnSO}_4 \cdot \text{H}_2\text{O}$, 99%, Acros Organics), boric acid (H_3BO_3 , Laboratory-grade, Fisher Scientific), sodium citrate dihydrate ($\text{C}_6\text{H}_5\text{Na}_3\text{O}_7 \cdot 2\text{H}_2\text{O}$, Fisher Scientific), saccharin, sodium salt hydrate, ($\text{C}_7\text{H}_6\text{NNaO}_4\text{S}$, 99%, Acros Organics), ethylene glycol ($\text{HOCH}_2\text{CH}_2\text{OH}$, Fisher Scientific), oxalic acid dihydrate ($\text{HO}_2\text{CCO}_2\text{H}$, 98%, Alfa Aesar). Deionized water (DI water, $18.2 \text{ M}\Omega \cdot \text{cm}$) was used to prepare all aqueous solutions. All analytical grade chemicals are purchased without further purification.

Catalysts synthesis

The one-pot electrodeposition (bottom-up) method was used to prepare the PdNiMn film. All electrolytes were prepared with ultrapure water ($18.2 \text{ M}\Omega \cdot \text{cm}$). The electrolyte bath for electrodeposition was prepared by dissolving 0.3 M NiSO_4 , 0.1 M NiCl_2 , 0.007 M MnSO_4 , 1 M H_3BO_3 , 2 mM PdCl_2 solution dissolved in hydrochloric acid ($2 \text{ mg} \cdot \text{mL}^{-1}$), 0.05 M sodium citrate, and 0.01 M saccharin in DI water and then stirring for 30 mins at room temperature. Then the electrodeposition was conducted in a homemade electroplating cell using stainless steel as the working electrode and platinum (Pt) mesh as the counter electrode at $20 \text{ mA} \cdot \text{cm}^{-2}$ for 15 mins. The PdNiMn film was peeled off from stainless steel after the electrodeposition. The subsequent anodization was treated at 60 V for 10 mins with PdNiMn film as working and Pt as counter electrodes in an electrolyte consisting of 0.2 M oxalic acid and 2 M DI water in ethylene glycol. Then the obtained surface oxygenated PdNiMn-PF was washed with DI water and ethanol several

times followed by air drying. The key role of oxalic acid and H₂O in the synthesis procedure is to etch the surface to form a porous structure and provide O for the formation of oxide, respectively. and the electrolyte compositions (ratio of oxalic acid and water) were adjusted to control the degree of oxygenation. and Other control catalysts were fabricated with the same electrodeposition method, except for PdNi film without adding MnSO₄ and NiMn film without adding PdCl₂. And the PdNiMn-MPF was prepared by directly immersing the PdNiMn film into 0.5 M H₂SO₄ solution for 15 mins.

Structural characterizations

The structure and morphology of the materials were characterized by scanning electron microscope (SEM, ZEISS ultra-55) and high-resolution transmission electron microscope (HRTEM) with energy-dispersive X-ray spectroscopy (EDS) mapping (Cs-corrected Titan 80-300 TEM). The compositions of the materials were determined by X-ray fluorescence (XRF) spectrometer (PANalytical Epsilon). The crystal structure was characterized by X-ray diffraction (XRD, Panalytical X'celerator multi-element detector with Cu K α radiation source, $\lambda = 1.54056$ Å). The chemical state/fingerprints information was investigated by X-ray photoelectron spectroscopy (XPS Escalab 250Xi) and the calibration was referenced to adventitious C 1s, C-C peak at a binding energy of 284.8 eV. The work function was measured via Ultraviolet Photoelectron Spectroscopy (UPS) with a photon energy of 21.22 eV (He-I). Raman Spectroscopy (Horiba LabRAM confocal Raman spectroscopy) with a 532 nm green laser was used to probe the surface metal oxide and the calibrated Si wafer Raman band is around 520 cm⁻¹. X-ray absorption spectroscopy (XAS) measurements were performed at beamline 12BM at Advanced Photon Source, Argonne National Laboratory. Pd K-edge, Ni K-edge, and Mn K-edge X-ray absorption near edge structure (XANES) and extended X-ray absorption fine structure (EXAFS) data were

collected in fluorescence mode. All thin film samples and the metal references were measured in the same beamtime. All those Pd, Ni, and Mn energy was calibrated to the standard pure metal edge when performing the XAS experiments. Background subtraction and normalization were performed with the Athena software package. Wavelet Transfer was performed by Harald Funke and Marina Chukalina (HAMA) Fortran Version from the European synchrotron radiation facility^{1, 2}. The k-range for the Wavelet transfer with Morlet function was selected from 3\AA^{-1} to 12\AA^{-1} and a k-weight of 3 was used. The frequency of the sine and cosine functions was set to the two times of the critical radius distance (e.g., $\sim 2.2\text{\AA}$ for Pd) which we are interested in, and the Gaussian peak half-width was set to 1. The k-range for the Fourier Transfer is the same as Wavelet transfer, which is 3\AA^{-1} to 12\AA^{-1} by using the Hanning function.

Computational method

The first principles density functional theory (DFT)^{3, 4} calculations were performed using the Vienna ab initio simulation package (VASP)^{5, 6} software. The energy cutoff was set as 500 eV for plane wave expansion. The core electrons were described by projector augmented wave (PAW)^{7, 8} pseudopotential. The Perdew, Burke, and Ernzerhof (PBE) functionals of generalized gradient approximation (GGA)⁹ were used to describe the electronic exchange and correlation energy. p(4×4) Pd(111) slab model containing four Pd layers was used in our calculations. The Pd atoms in the bottom two layer were fixed during structural relaxation. In the DFT structure optimization calculations, the atomic positions were allowed to relax until the force on each ion fell below 0.02 eV/Å. The Brillouin Zone was sampled with a 3×3×1 k-point mesh for Pd(111) and Mn-Pd(111). A vacuum layer of 18 Å perpendicular to the slab was added to avoid the interaction between periodic images. The zero-point energy, entropy, and solvation correction were considered in all calculations of ORR intermediate adsorption.¹⁰

Electrochemical measurements

All electrochemical measurements were tested by the electrochemical workstation (CHI 760E) in a standard three-electrode system at room temperature, in which the as-prepared catalysts were stuck to the rotating ring-disk electrode (RRDE, 0.2475 cm² disk area and 0.1866 cm² Pt ring area) as working electrode, carbon rod as the counter electrode, and Ag/AgCl (4 M KCl) as the reference electrode. The electrolytes used in this work for measuring ORR and OER are 0.1 M KOH (pH=13.38) and 1 M KOH (pH=13.81) respectively. All potentials were calculated and referred to the reversible hydrogen electrode (RHE). The pH of the electrolyte was tested by the SevenCompact pH meter. Oxygen reduction reaction (ORR)-related experiments were recorded and analyzed by conducting cyclic voltammetry (CV) and linear sweep voltammetry (LSV). All LSV curves in this work were shown without IR correction.

The commercial Pd/C (10 wt% of 8-nm Pd nanoparticles on activated carbon, Aldrich) was used as the control catalyst for the ink preparation, by dispersing 5.0 mg Pd/C in the solution of Nafion/IPA/water/ (40 μL/480 μL/480 μL) in 2 mL plastic vial under sonication for 30 mins. The 7.5 μL catalyst ink was dropped on the RRDE and dried in the air naturally.

The overall electrochemical active surface area (*ECSA*) of porous films was calculated according to the electrochemical double-layer capacitance (*C_{dl}*). The *C_{dl}* was determined by CV curves in the non-Faradic region at various scan rates from 10 mV/s to 100 mV/s:

$$C_{dl}=J/\nu \quad (E1)$$

where *J* is the double layer current densities from CV curves, *ν* is the scan rate. The *ECSA* can be calculated from the equation:

$$ECSA=C_{dl}/C_s \quad (E2)$$

where C_s is the capacitance of an atomically smooth planar surface of the material per unit area under identical electrolyte conditions.

The electrochemical active surface area of Pd ($EASA_{Pd}$) of the catalysts were calculated from CV curves measured in N_2 -saturated 0.1 M KOH electrolyte at a scan rate (ν) of 50 mV/s, by integrating the charge (Q_{Hads}):

$$EASA_{Pd} = \frac{Q_{Hads}}{210 \mu C \cdot cm^{-2} \times m_{Pd}} \quad (E3)$$

where m_{Pd} is the estimated weight recorded from the SEM-EDS result.

The Koutecky-Levich (K-L) plots were used to calculate the electron transfer number of ORR:

$$\frac{1}{i} = \frac{1}{i_d} + \frac{1}{i_k} = \frac{1}{B\omega^{1/2}} + \frac{1}{i_k} \quad (E4)$$

$$B = 0.62nFC_0(D_0)^{\frac{2}{3}}\nu^{-\frac{1}{6}} \quad (E5)$$

where i_k is the kinetic current, i_d is the diffusion-limiting current, i is the measured total current from LSV curves, ω (rad/s) is the angular velocity of the disk ($\omega = 2\pi N$, N is the rotation speed), n is the electron transfer number, F is the Faraday constant ($F = 96485$ C/mol), C_0 is the bulk concentration of O_2 in 0.1 M KOH electrolyte ($C_0 = 1.2 \times 10^{-6}$ mol/cm³), D_0 is the diffusion coefficient of O_2 in 0.1 M KOH electrolyte ($D_0 = 1.9 \times 10^{-5}$ cm²/s), ν is the kinematic viscosity of 0.1 M KOH electrolyte ($\nu = 0.01$ cm²/s).

The electron transfer number (n) and hydrogen peroxide yield ($\chi_{H_2O_2}$ (%)) were calculated based on the disk current (I_{disk}) and ring current (I_{ring}):

$$n = 4 I_{disk} / (I_{disk} + I_{ring}/N) \quad (E6)$$

$$\chi_{(H_2O_2)} = (200 I_{ring}/N)/((I_{disk} + I_{ring}/N)) \quad (E7)$$

where $N = 0.37$ is the calculated current collection efficiency of the Pt ring.

The electrochemical stability test for ORR was conducted using chronoamperometry (CA) method by continuously collecting i-t plot under 0.6 V (V vs RHE) in O_2 -saturated 0.1 M KOH electrolyte for 12 h.

ZAFB measurements

Aqueous ZAFBs were assembled with Zn plates as the anodes and PdNiMnO as cathodes with ambient air naturally flowing into the electrolyte, and the small peristaltic pump (NKCP-S10-B, K KAMOER) was set at a velocity of $30 \text{ mL} \cdot \text{min}^{-1}$. The electrolyte used in ZAFB consisted of 6 M KOH and 0.2 M Zn $(\text{CH}_3\text{COO})_2$. The exposed area of the electrode to the electrolyte was 0.5 cm^2 . The open-circuit voltage (OCP) was recorded with the multimeter, and the polarization curves were scanned at $5 \text{ mV} \cdot \text{s}^{-1}$ on a CHI 760E electrochemical workstation to measure the peak power density. The rate performance was evaluated by discharging the ZAFBs at various current densities ($5 \text{ mA} \cdot \text{cm}^{-2}$ to $50 \text{ mA} \cdot \text{cm}^{-2}$), and the rate performance of ZAFB (PdNiMnO) was recorded after running over 200h of charge/discharge cycles in order to activate the catalyst. The stability of ZAFBs was measured on a LAND station (CT2001A) with alternatively charging and discharging at $10 \text{ mA} \cdot \text{cm}^{-2}$ for 30 mins. The control ZAFB (Pt/C-RuO₂) was assembled by dropping the catalyst ink of Pt/C-RuO₂ (mass ratio = 1:1) to the carbon paper and naturally drying in air. A green LED lamp was lightened up by using two ZAFBs in series. The specific capacity of ZAFBs was calculated based on the consumed mass of the Zn plate. The voltage gap of ZAFBs is defined as the potential difference between the charge potential and discharge potential at $10 \text{ mA} \cdot \text{cm}^{-2}$ read from the last cycle.

Supporting Figures

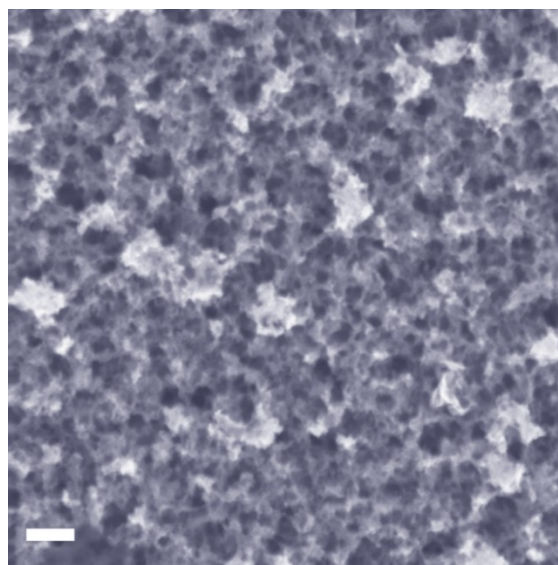


Figure S1. Top-view SEM image of PdNiO-PF. Scale bar: 200 nm.

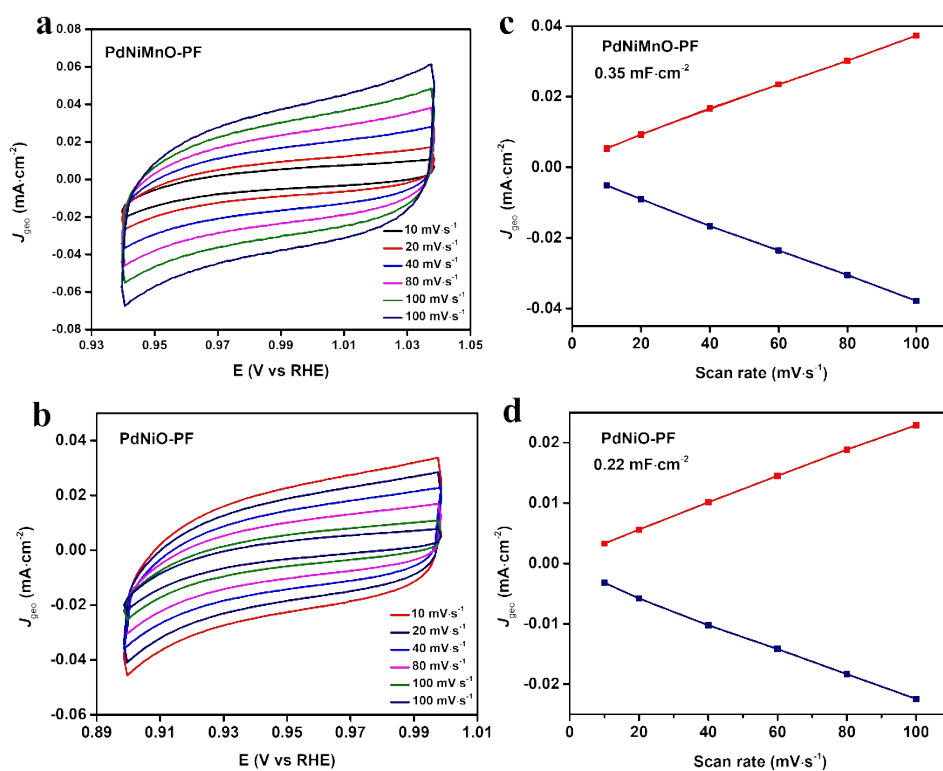


Figure S2. Electrochemical active surface area (ECSA) of PdNiMnO-PF and PdNiO-PF. Corresponding (a-b) CV curves and (c-d) calculated capacitance.

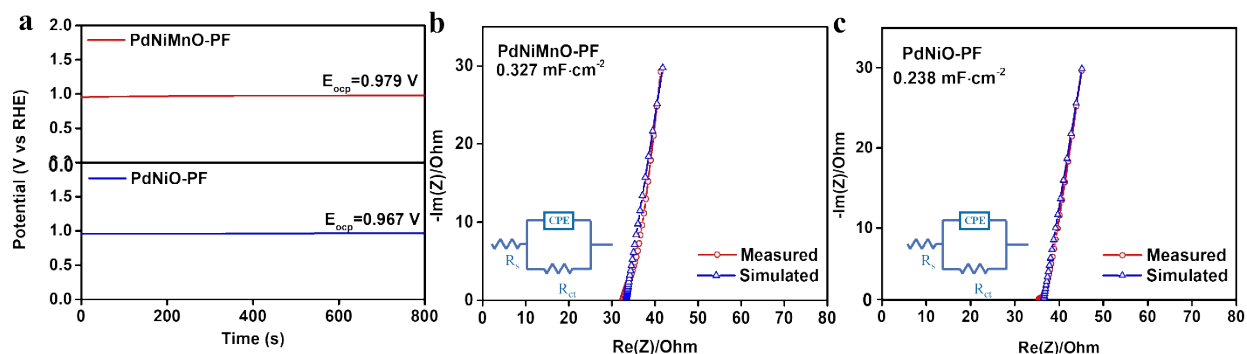


Figure S3. (a). Open circuit potential (OCP) of PdNiMnO-PF and PdNiO-PF. Nyquist plots for (b) PdNiMnO-PF and (c) PdNiO-PF measured in 0.1 M KOH at the open-circuit voltage (OCP) for estimating electrical double layer capacitance (EDLC).

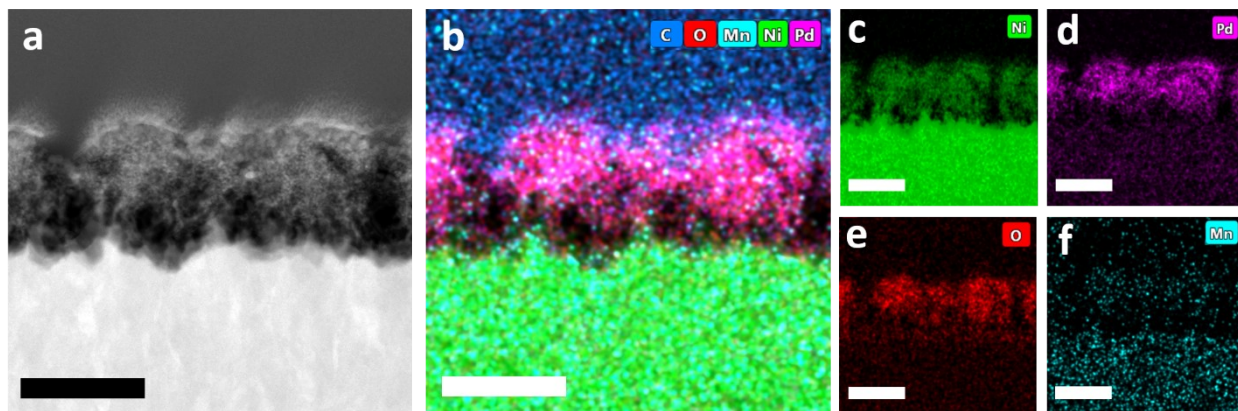


Figure S4. (a) STEM-HAADF image of PdNiMnO-PF in the cross-sectional view, (b) the corresponding overlapped EDS elemental mapping, and the corresponding individual EDS elemental mapping for (c) Ni, (d) Pd, (e) O, and (f) Mn, respectively. Scale bar: 200 nm.

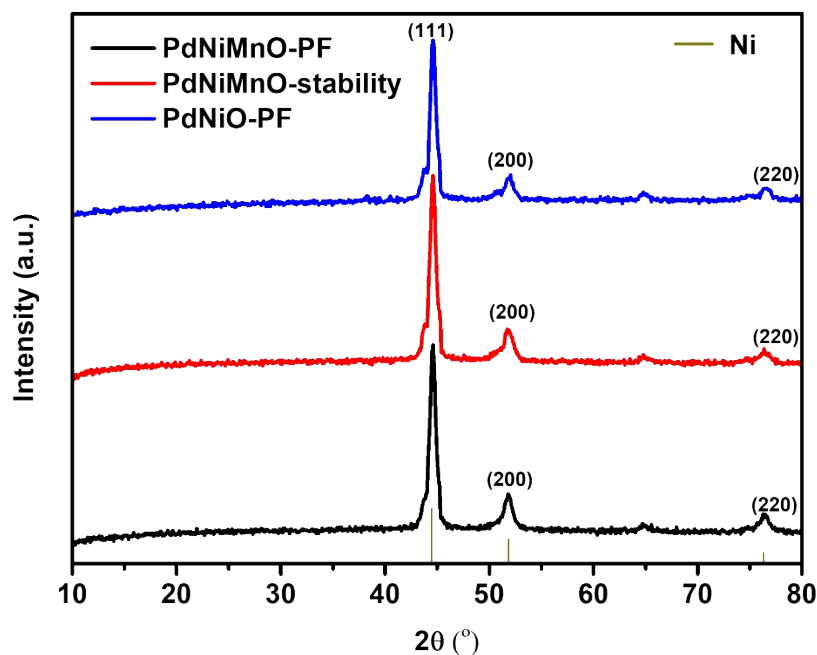


Figure S5. X-ray diffraction (XRD) pattern of PdNiMnO-PF, PdNiMnO-stability, and PdNiO-PF.

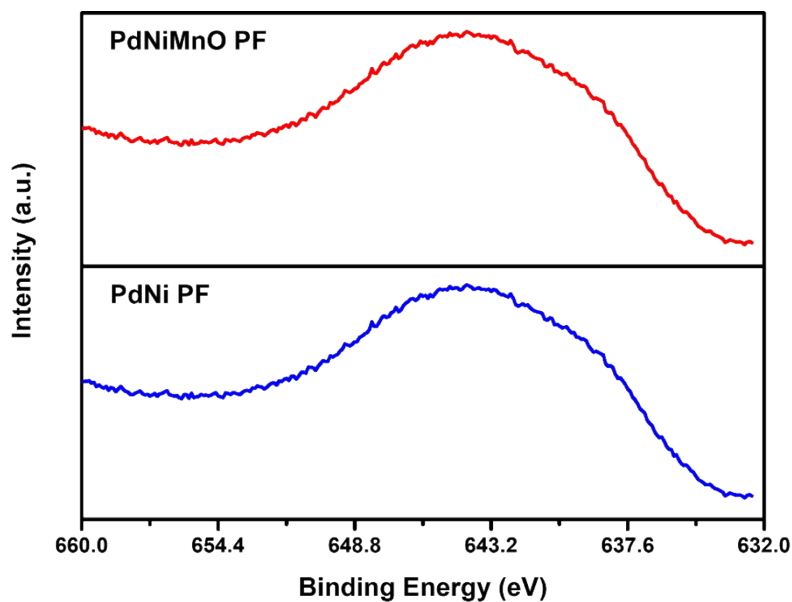


Figure S6. XPS spectra of Ni LMM Auger peak for PdNiMnO-PF and PdNiO-PF, overlapping with Mn 2p.

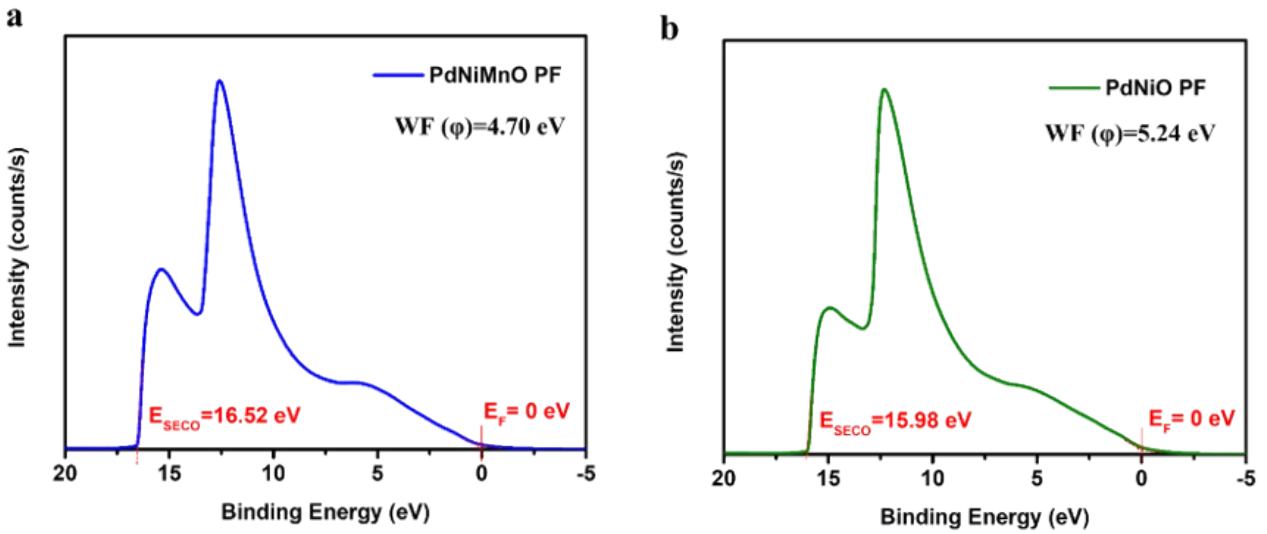


Figure S7. Ultraviolet photoelectron spectroscopy (UPS) spectra of (a) PdNiMnO-PF and (b) PdNiO-PF.

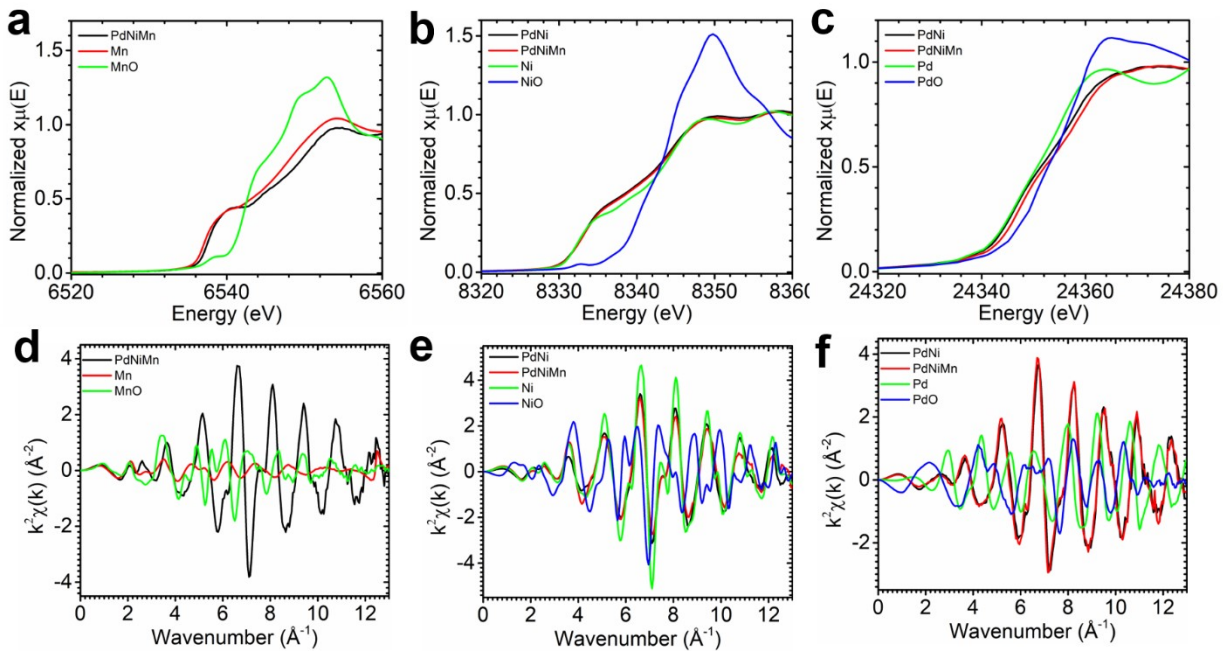


Figure S8. X-ray absorption near edge structure for (a) Mn K-edge (b) Ni K-edge (c) Pd K-edge. Extended X-ray absorption fine structure k-space for (d) Mn K-edge (e) Ni K-edge (f) Pd K-edge.

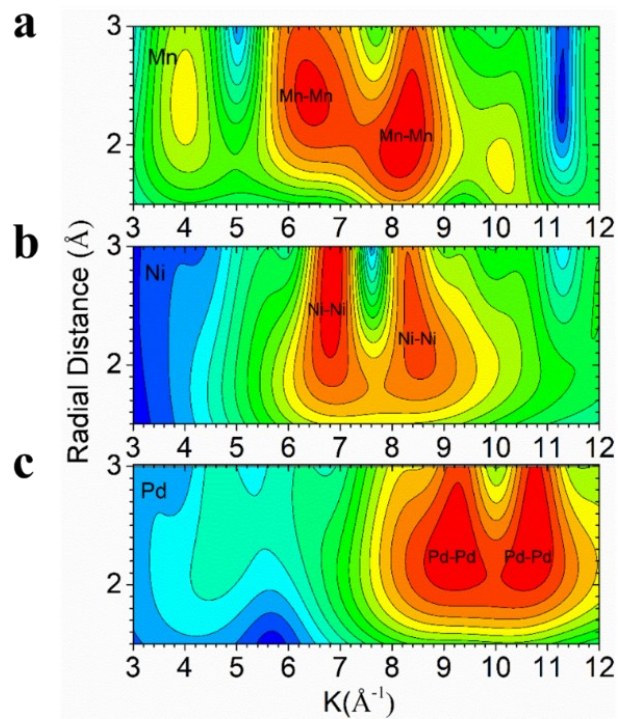


Figure S9. Wavelet Transform of metallic (a) Mn, (b) Ni, and (c) Pd (from top to bottom).

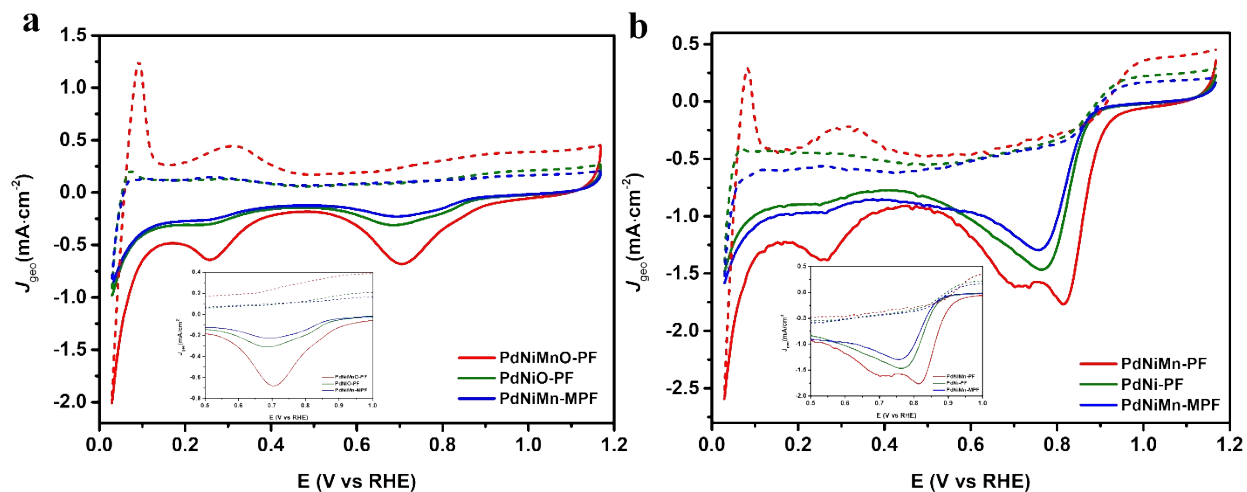


Figure S10. Comparison of cyclic voltammetry (CV) curves of PdNiMnO-PF, PdNiO-PF, and PdNiMn-MPF in (a) N₂- and (b) O₂-saturated 0.1 M KOH electrolyte.

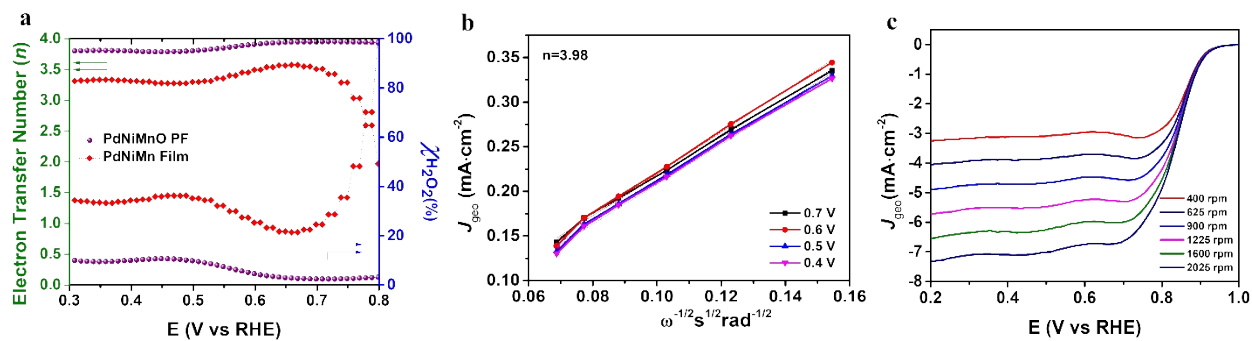


Figure S11. ORR performance of PdNiMnO-PF. **(a)** Electron transfer number (n) and hydrogen peroxide production rate ($\chi_{\text{H}_2\text{O}_2}$ (%)) as a function of applied potentials. **(b)** K-L plot at different potentials. **(c)** Linear sweep voltammetry (LSV) curves at a scan rate of $5 \text{ mV}\cdot\text{s}^{-1}$.

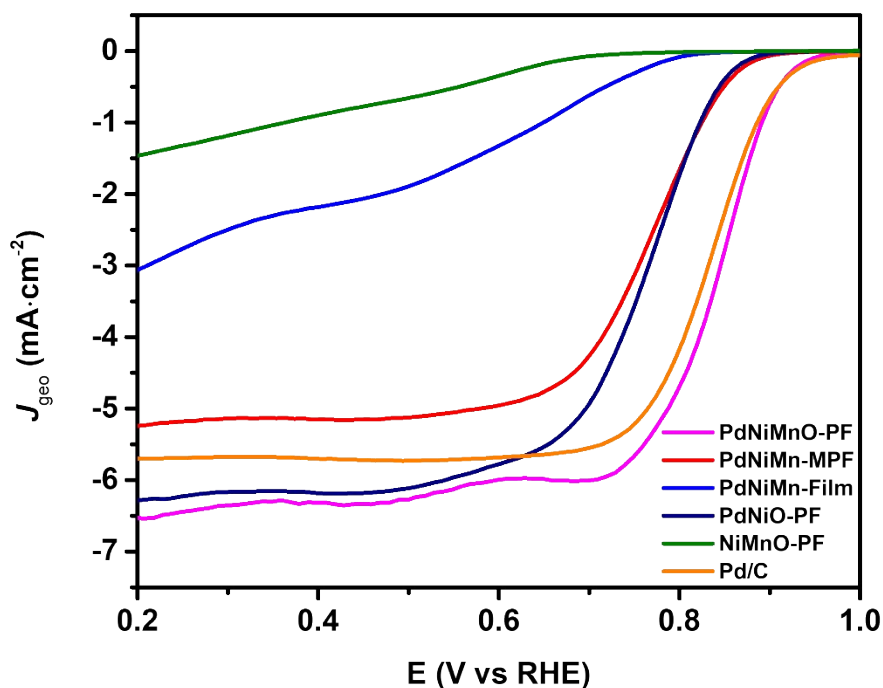


Figure S12. Comparison of LSV curves of PdNiMnO-PF with other control catalysts with 1600 rpm at a scan rate of $5 \text{ mV}\cdot\text{s}^{-1}$.

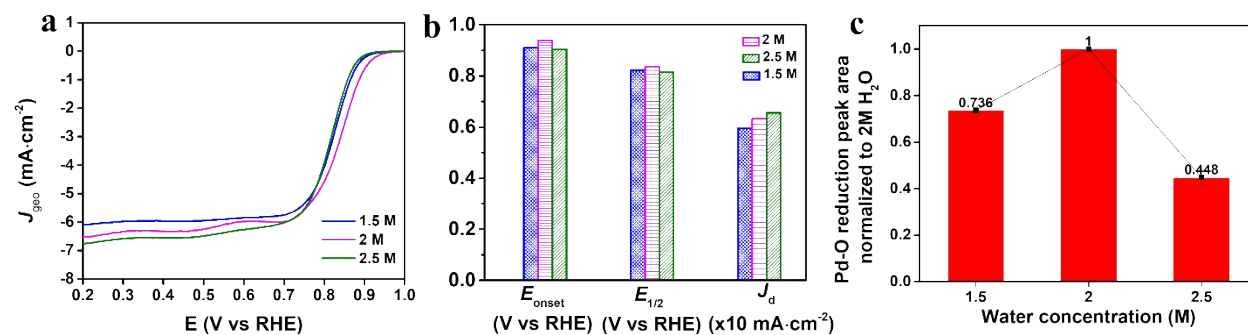


Figure S13. Comparison of (a) LSV curves and (b) E_{onset} , $E_{1/2}$, and J_{lim} of PdNiMnO-PF prepared in the electrolytes with different H₂O amounts. (c) Comparison of Pd-O reduction area integrated from CV curves for the catalysts synthesized in the electrolytes with different H₂O concentrations, normalized to the optimized one (2 M).

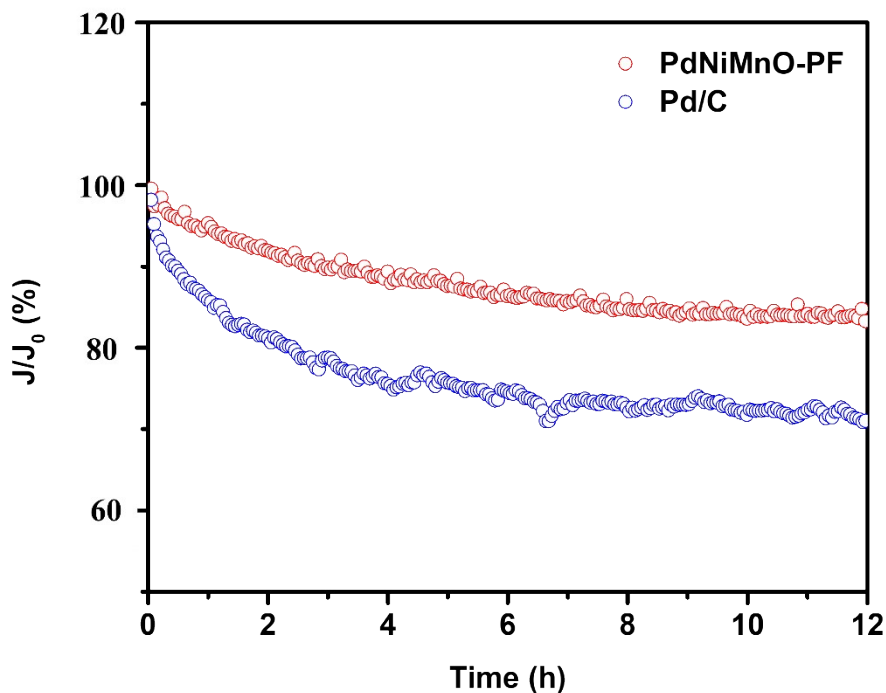


Figure S14. Chronoamperometric (CA) ORR stability test of PdNiMnO-PF and Pd/C.

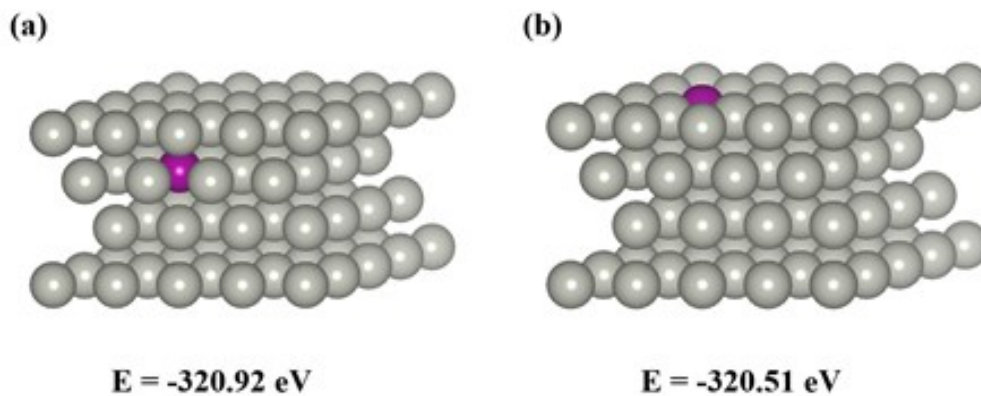


Figure S15. Atomistic structure of Mn-Pd(111) surface. (a) doped Mn in the sublayer, and (b) doped Mn in the outermost layer. In these figures, the grey, and purple balls represent Pd and Mn atoms, respectively. The predicted system energies are presented below the two configurations.

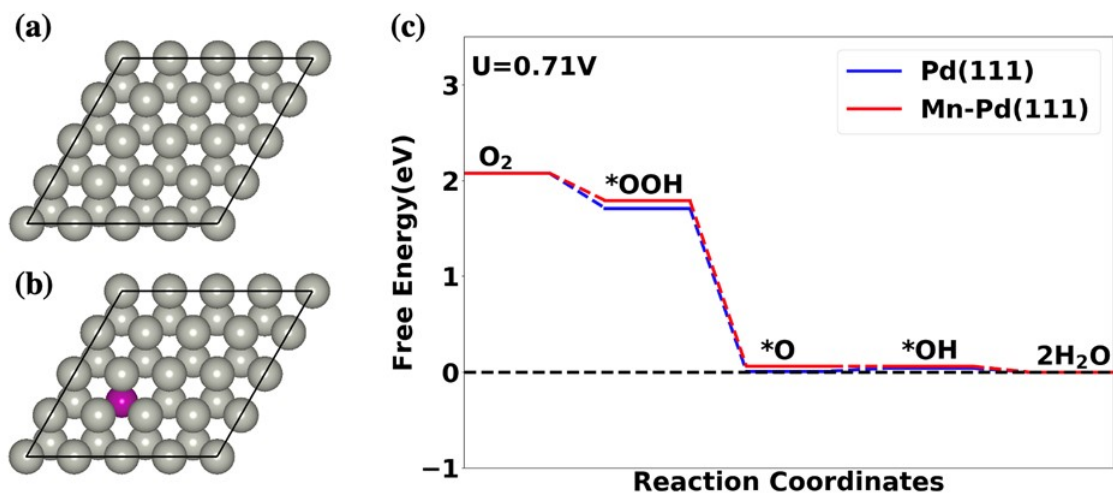


Figure S16. Atomistic structure of (a) Pd(111) and (b) Mn-Pd(111) surface. In these figures, the grey and purple balls represent Pd and Mn atoms, respectively. (c) Calculated free energy evolution for ORR through $4e^-$ associative pathway on the Pd(111) and Mn-Pd(111) under an electrode potential of $U = 0.71 \text{ V}$.

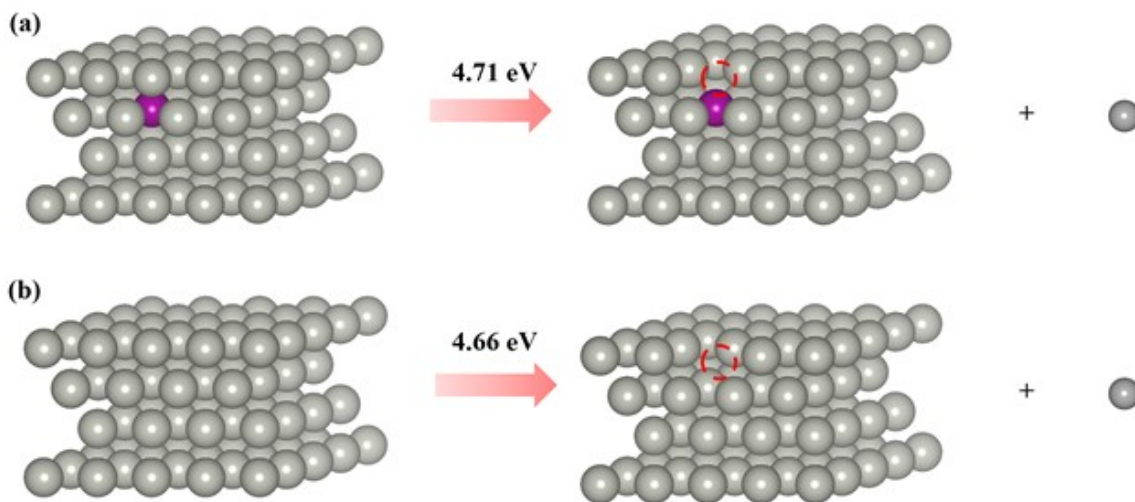


Figure S17. Atomistic structures of simulation models for demetallation of Pd atom from the outermost layer of (a) Pd(111) and (b) Mn-Pd(111). The grey and purple balls represent Pd and Mn atoms, whereas the red dash circle represents a Pd vacancy, respectively.

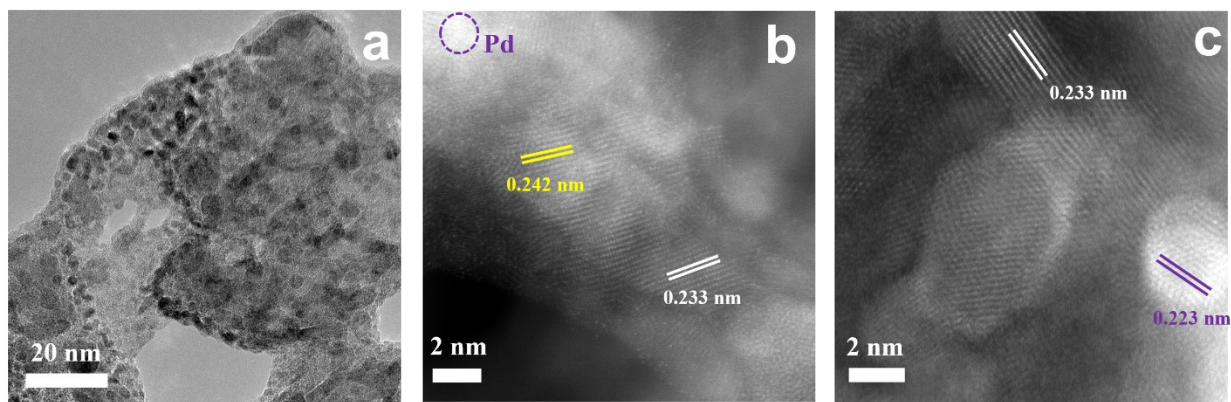


Figure S18. HRTEM image (a) and STEM-HAADF images (b-c) of PdNiMnO-PF after stability test.

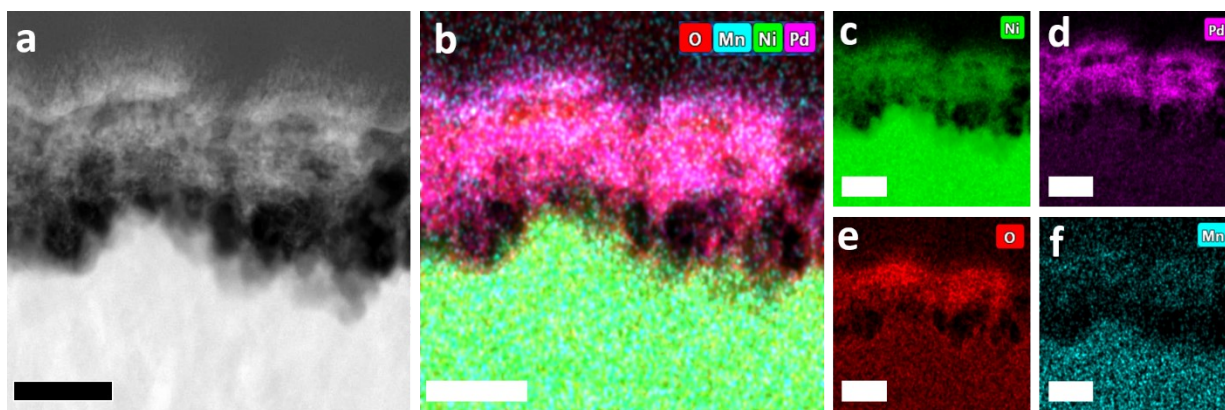


Figure S19. (a) Cross-sectional STEM-HAADF image of PdNiMnO-PF after stability test, (b) the corresponding overlapped EDS elemental mapping, and the corresponding individual EDS elemental mapping for (c) Ni, (d) Pd, (e) O, and (f) Mn, respectively. Scale bar: 100 nm.

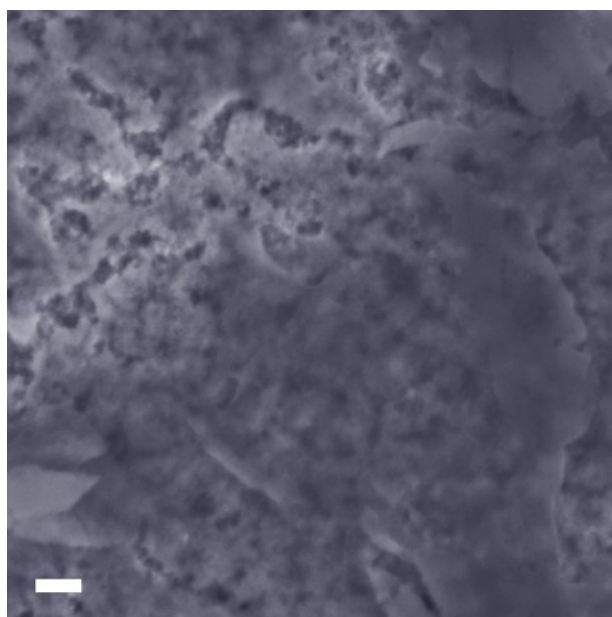


Figure S20. Top-view SEM image of PdNiMnO-PF after stability test. Scale bar: 200 nm.

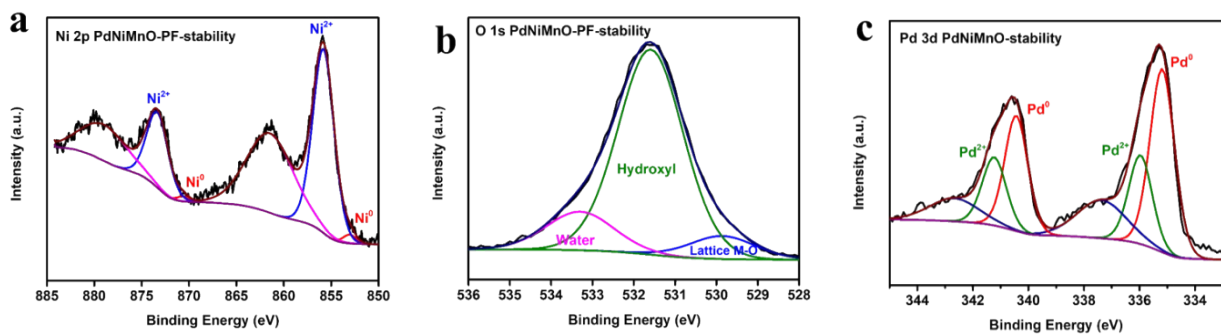


Figure S21. XPS spectra of PdNiMnO-PF after stability test. (a) Ni 2p, (b) O 1s, and (c) Pd 3d.

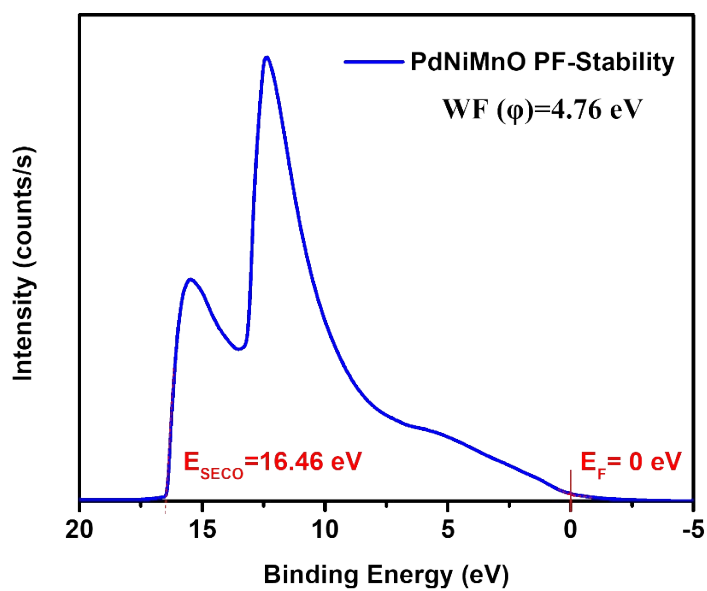


Figure S22. UPS spectrum of PdNiMnO-PF after stability test.

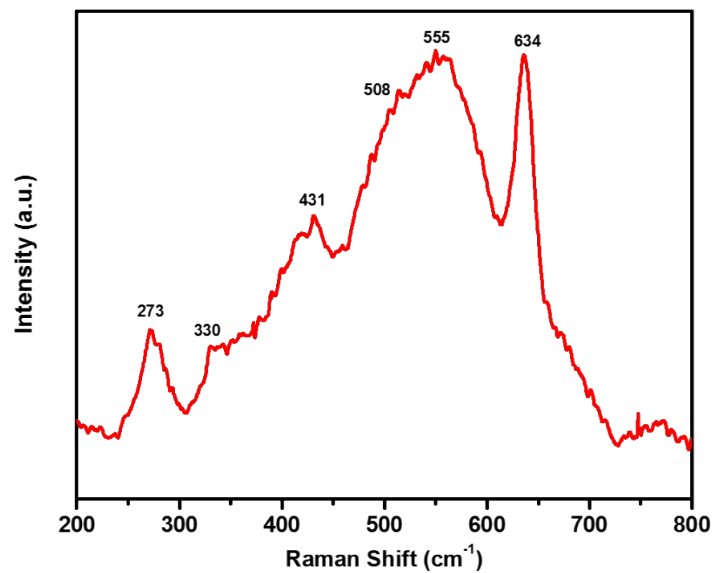


Figure S23. Raman spectrum of PdNiMnO-PF after stability test.

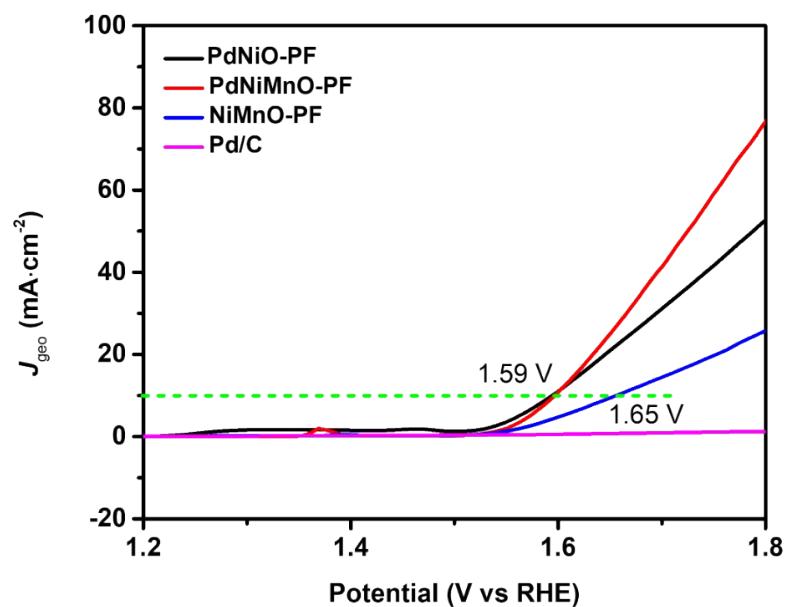


Figure S24. OER LSV polarization curves of PdNiMnO-PF and other control catalysts tested in 1 M KOH electrolyte at a scan rate of $5 \text{ mV} \cdot \text{s}^{-1}$.

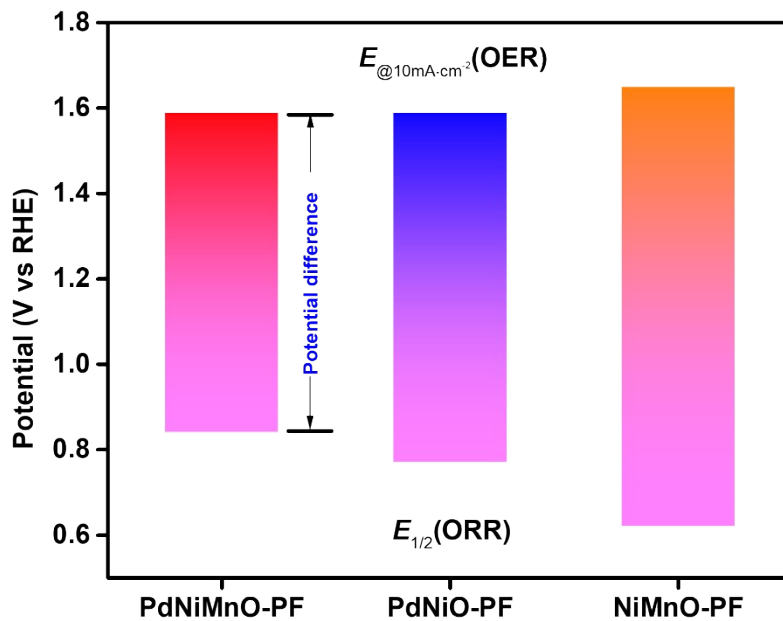


Figure S25. An overall potential difference of ORR/OER performance as a bifunctional catalyst for PdNiMnO-PF and other control samples.

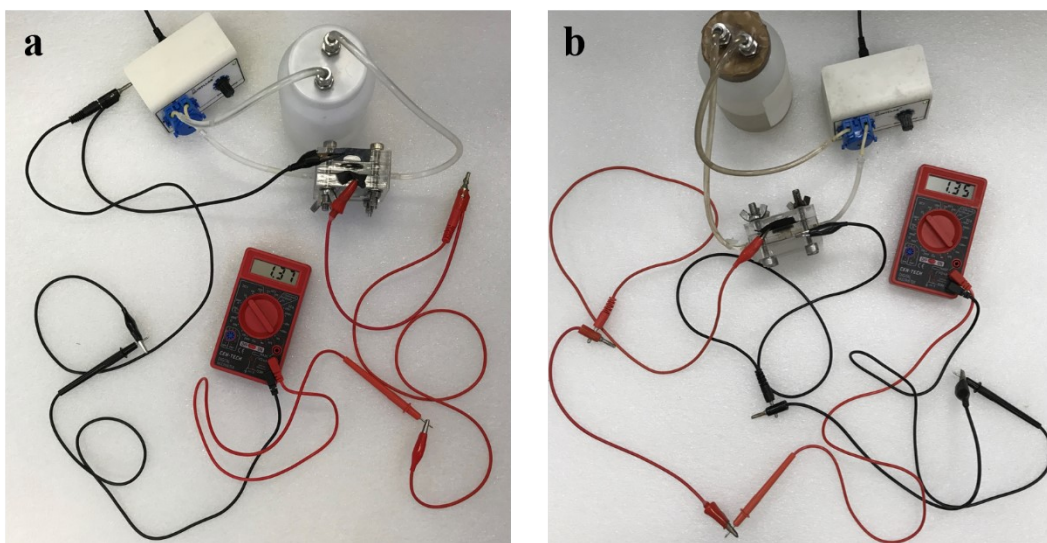


Figure S26. Open circuit voltage of ZAFBs. (a) PdNiMnO and (b) Pt/C-RuO₂ as the cathode catalyst.

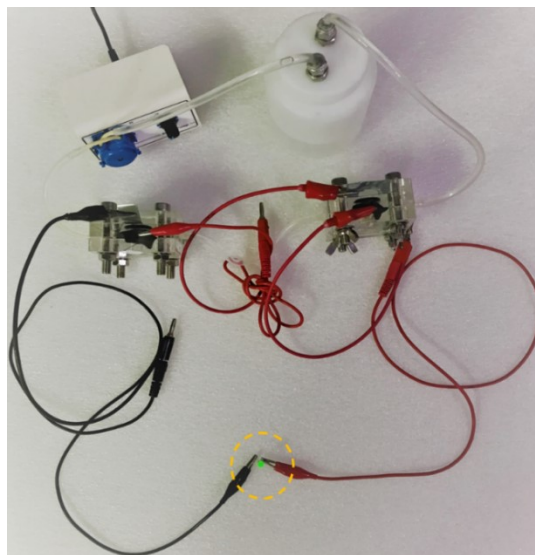


Figure S27. Green LED bulb (forward voltage: 1.8-2.0 V) lightened up by two ZAFBs in series with PdNiMnO as the cathode catalyst.

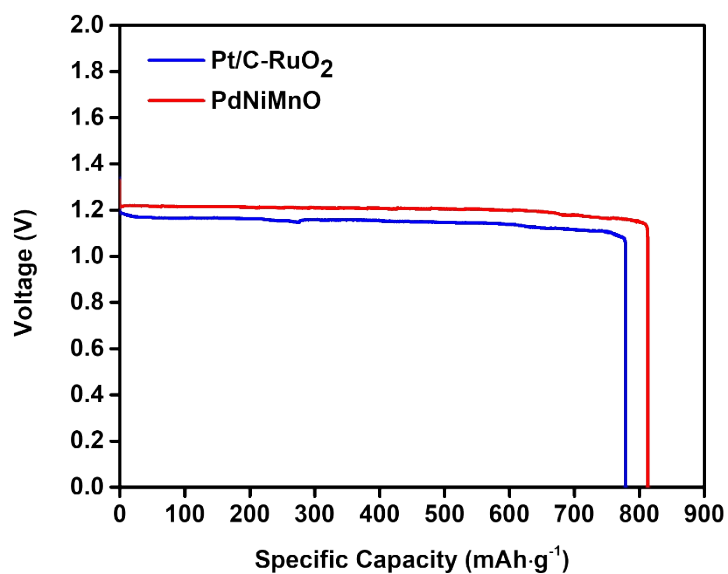


Figure S28. Specific capacity of ZAFBs using PdNiMnO and Pt/C-RuO₂ as cathode catalyst at 10 mA·cm⁻².

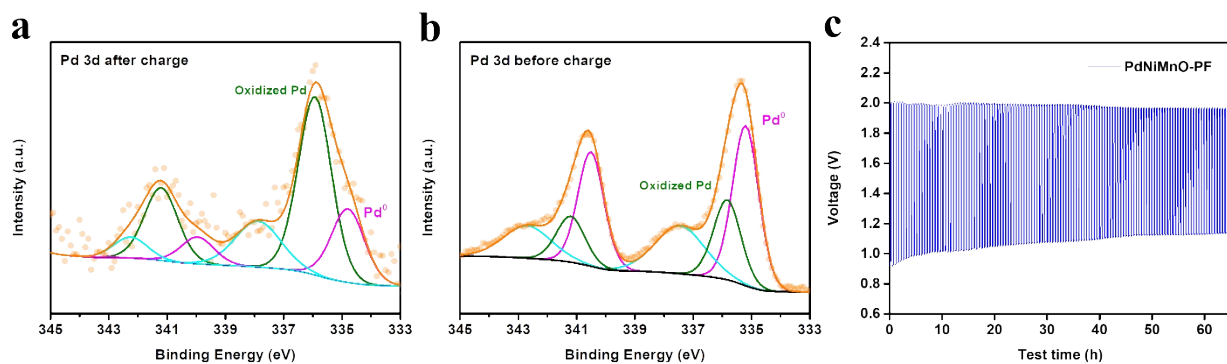


Figure S29. High-resolution XPS Pd 3d spectra of (a) after charge and (b) before charge process for 65 hours (130 cycles) of PdNiMnO-PF as the cathode in the zinc-air battery. (c) Cyclic charge/discharge performance of zinc-air battery at the current density of $10 \text{ mA}\cdot\text{cm}^{-2}$.

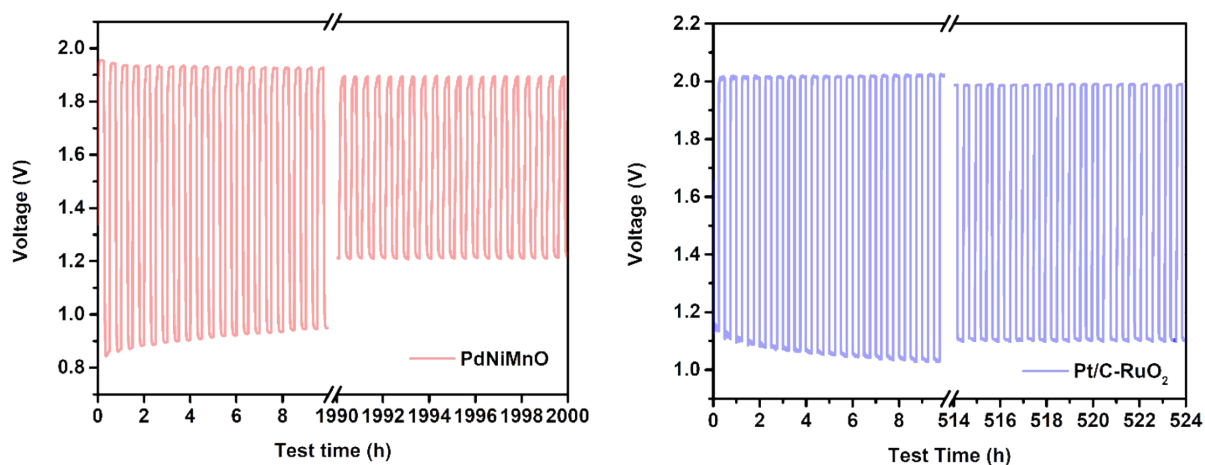


Figure S30. Galvanostatic discharge-charge performance of (a) PdNiMnO and (b) Pt/C-RuO₂ ZAFBs for the 1st and last 10 hours at $10 \text{ mA}\cdot\text{cm}^{-2}$.

Supporting Tables

Table S1. Elemental compositions of PdNiMnO-PF and PdNiO-PF estimated from XRF.

Catalysts	Ni (at%)	Pd (at%)	Mn (at%)
PdNiMnO-PF	99.25	0.41	0.33
PdNiO-PF	99.64	0.36	/

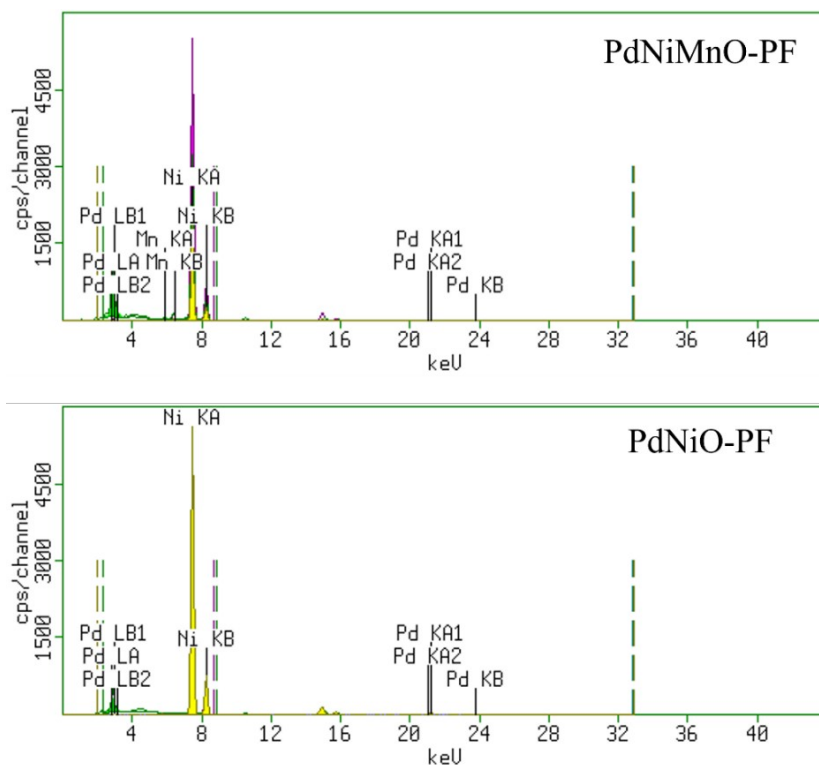


Table S2. Elemental compositions of PdNiMnO-PF estimated from SEM-EDS.

Element Line	wt%	at%
Mn K	0.2 \pm 0.1	0.2 \pm 0.1
Ni K	93.8 \pm 3.1	92.2 \pm 3.6
Pd L	4.6 \pm 2.6	2.5 \pm 1.4
O K	1.45 \pm 0.65	5.1 \pm 2.3

Table S3. ORR performance of PdNiMnO-PFs with different anodization conditions.

H ₂ O/oxalic acid	E_{onset} (@0.1 mA/cm ²)	$E_{1/2}$ (@1600 rpm)	J_d (@1600 rpm)
1.5 M/0.2 M	0.91 V	0.823 V	5.96 mA·cm ⁻²
2 M/0.2 M	0.94 V	0.836 V	6.32 mA·cm ⁻²
2.5 M/0.2 M	0.905 V	0.814 V	6.56 mA·cm ⁻²

Table S4. Elemental composition analysis of PdNiMnO-PF before and after stability test.

TEM-EDX composition data

Catalyst	Pd (at. %)	Ni (at. %)	Mn (at. %)
Fresh catalyst	26.5	73	0.5
Cycled catalyst	23.8	75.8	0.4

XPS composition data

Catalyst	Pd (at. %)	Ni (at. %)
Fresh catalyst	22.5	77.5
Cycled catalyst	21.67	78.33

Table S5. ZAFBperformance of PdNiMnO compared with state-of-the-art catalysts.

Category	Catalysts	Voltage	Power	Current	Stability	Ref.
		Gap ($\Delta E/V$)	Density (mW·cm ⁻²)	Density (mA·cm ⁻²)		
PGM-based catalysts	PdNiMnO	0.69	211.6	10	2000 h (4000 cycles)	This work
	SA-PtCoF	0.9	125	10	240 h	11
	Pt-SCFP/C-12	0.86	122	5	80 h (10 mins per cycle)	12
	PdMo bimetalallene	0.78	154.2	10	500h	13

	Pd/FeCo	0.9	117	10	200 h (400 cycles)	14
carbon-based composites	CFP@NSC-900	0.9	45	5	55 h (60 mins per cycle)	15
	FeCo/N-DNC	0.72	115	10	30 cycles/20 mins per cycle	16
	Co ₉ S ₈ /CD@NSC	0.66	92.7	10	125 h	17
	HPNSC	0.88	82.6	10	88 h (2 hour per cycle)	18
	FeS/Fe ₃ C@N-SC	0.93	63	20	24 h	19
	BN/C&RuO ₂	0.9	115	5	14 days (1000 cycles)	20
	NiFe@NBCNT	0.8	82	10	200 cycle/130 h	21
transitional metal-based catalysts	MnO ₂ -NiFe	0.69	93.95	10	/	22
	Ni-Fe-MoN NTs	0.98	118	10	20 h	23
	N-NiO	0.9	112.3	24	160 h (240 cycles)	24
single-atom catalyst	Fe-N _x -C	0.92	96	10	250 h, 500 cycles	25

References

1. H. Funke, A. C. Scheinost and M. Chukalina, *Physical Review B*, 2005, **71**, 094110.
2. H. Funke, M. Chukalina and A. C. Scheinost, *Journal of synchrotron radiation*, 2007, **14**, 426-432.
3. P. Hohenberg and W. Kohn, *Physical Review*, 1964, **136**, B864-B871.
4. W. Kohn and L. J. Sham, *Physical Review*, 1965, **140**, A1133-A1138.
5. G. Kresse and J. Furthmüller, *Computational Materials Science*, 1996, **6**, 15-50.
6. G. Kresse and J. Hafner, *Physical Review B*, 1993, **47**, 558-561.
7. P. E. Blöchl, *Physical Review B*, 1994, **50**, 17953-17979.
8. G. Kresse and D. Joubert, *Physical Review B*, 1999, **59**, 1758-1775.
9. J. P. Perdew, K. Burke and M. Ernzerhof, *Physical Review Letters*, 1996, **77**, 3865-3868.
10. L. Wang, W. Gao, Z. Liu, Z. Zeng, Y. Liu, M. Giroux, M. Chi, G. Wang, J. Greeley, X. Pan and C. Wang, *ACS Catalysis*, 2018, **8**, 35-42.
11. Z. Li, W. Niu, Z. Yang, N. Zaman, W. Samarakoon, M. Wang, A. Kara, M. Lucero, M. V. Vyas, H. Cao, H. Zhou, G. E. Sterbinsky, Z. Feng, Y. Du and Y. Yang, *Energy Environ. Sci.*, 2020, **13**, 884-895.
12. X. Wang, J. Sunarso, Q. Lu, Z. Zhou, J. Dai, D. Guan, W. Zhou and Z. Shao, *Adv. Energy Mater.*, 2020, **10**, 1903271.
13. M. Luo, Z. Zhao, Y. Zhang, Y. Sun, Y. Xing, F. Lv, Y. Yang, X. Zhang, S. Hwang, Y. Qin, J.-Y. Ma, F. Lin, D. Su, G. Lu and S. Guo, *Nature*, 2019, **574**, 81-85.
14. F. Pan, Z. Li, Z. Yang, Q. Ma, M. Wang, H. Wang, M. Olszta, G. Wang, Z. Feng, Y. Du and Y. Yang, *Adv. Energy Mater.*, 2021, **11**, 2002204.
15. Y. Cheng, Y. Guo, N. Zhang, S. Tao, Z. Liao, Y. Wang and Z. Xiang, *Nano Energy*, 2019,

- 63**, 103897.
16. G. Fu, Y. Liu, Y. Chen, Y. Tang, J. B. Goodenough and J.-M. Lee, *Nanoscale*, 2018, **10**, 19937-19944.
 17. P. Zhang, D. Bin, J.-S. Wei, X.-Q. Niu, X.-B. Chen, Y.-Y. Xia and H.-M. Xiong, *ACS Appl. Mater. Interfaces*, 2019, **11**, 14085-14094.
 18. Y. Cheng, Y. Wang, Q. Wang, Z. Liao, N. Zhang, Y. Guo and Z. Xiang, *J. Mater. Chem. A*, 2019, **7**, 9831-9836.
 19. F. Kong, X. Fan, A. Kong, Z. Zhou, X. Zhang and Y. Shan, *Adv. Func. Mater.*, 2018, **28**, 1803973.
 20. R. Zhao, Q. Li, Z. Chen, V. Jose, X. Jiang, G. Fu, J.-M. Lee and S. Huang, *Carbon*, 2020, **164**, 398-406.
 21. D. Bin, B. Yang, C. Li, Y. Liu, X. Zhang, Y. Wang and Y. Xia, *ACS Appl. Mater. Interfaces*, 2018, **10**, 26178-26187.
 22. P. Wang, Y. Lin, L. Wan and B. Wang, *ACS Appl. Mater. Interfaces*, 2019, **11**, 37701-37707.
 23. C. Zhu, Z. Yin, W. Lai, Y. Sun, L. Liu, X. Zhang, Y. Chen and S.-L. Chou, *Adv. Energy. Mater.*, 2018, **8**, 1802327.
 24. J. Qian, X. Bai, S. Xi, W. Xiao, D. Gao and J. Wang, *ACS Appl. Mater. Interfaces*, 2019, **11**, 30865-30871.
 25. J. Han, X. Meng, L. Lu, J. Bian, Z. Li and C. Sun, *Adv. Func. Mater.*, 2019, **29**, 1808872.